

Impact-Induced Hardening on Dense Frictional Suspensions

Pradipto and Hisao Hayakawa

*Yukawa Institute for Theoretical Physics, Kyoto University,
Kitashirakawaoiwake-cho, Sakyo-ku, Kyoto 606-8502, Japan*

(Dated: May 7, 2020)

By employing the lattice Boltzmann method, we perform simulations that incorporate the contact between suspended particles as well as the free surface of the suspensions. Our simulation for a free falling impactor semi-quantitatively reproduces experimental counterparts, where the impactor bounces for high speed impact and high volume fraction shortly after the impact before subsequently sinks. We observe that the response depends on the radius of the impactor, which leads to fit our simulation data by a phenomenology based on the Hertzian contact theory. When the rebound takes place, a localized jammed region is formed as the sustaining force by frictional contact between particles. Furthermore, a persistent homology analysis elucidates the significance of the topological structure of force chains, where the total persistence of connected components correlates to the sustaining contact force.

Introduction.— One of typical examples of the non-Newtonian behavior of dense suspensions is the fact that running persons can stay afloat while walking persons sink. The solid-like response under fast impact and remaining fluid otherwise have also gained attraction for practical applications, such as protective vests. Such responses are often associated with the shear thickening, both the continuous (CST) and discontinuous (DST), in dense suspensions under simple shear flows. Nevertheless, the simple shear flow is different from the running on a liquid. The latter is regarded as one of impact problems in which response on the impact speed and the surface effect should be relevant. Some efforts have been made to reproduce the impact behavior through experiments [1–6]. Waitukaitis and Jaeger indicated that the added mass effect in solidified region after an impact is important [1]. The propagation of the dynamic jamming-front is also observed in a quasi-two-dimensional experiment for impact on a suspension [2]. Moreover, a series of penetration experiments under the constant speed condition [3–5] suggested that the added mass effect alone is insufficient to explain such huge resistance. Instead, they showed that the stress on the impactor increases as it approaches the bottom boundary. The importance of the bottom boundary characterized by depth of the suspensions H was also indicated from an experiment for free-falling impactor [6], where the bouncing motion of the impactor was observed shortly after the impact.

In order to extract microscopic information of two-dimensional dry granular materials in experiments, one could use photoelastic disks to visualize the force acting on each grain [7]. Similarly, numerical simulations have become an important tool to understand the microscopic mechanism behind exotic phenomena in suspensions since the motions of the suspended particles are not visible in three-dimensional experiments. One of the remarkable insights from simulations is that the frictional contacts between particles are important to observe the

DST under simple shear [8–12]. Nevertheless, particles-based simulation of a free-falling projectile onto suspensions has not been reported so far because of the difficulty to simulate suspensions with free-surface. Only recently, the first fluid-based simulation of suspensions under impact, as long as we know, has been conducted in Ref. [13], where the authors successfully reproduced various interesting processes for suspensions under impact, such as the viscoelastic response of a rotating wheel. Since, however, their fluid simulations with the aid of a constitutive equation cannot capture the particle dynamics, the mechanism behind impact-induced hardening in the microscopic level remains elusive. In this Letter, we utilize the lattice Boltzmann method (LBM) [14–16] to perform a simulation that can incorporate particle dynamics as well as the free surface of the suspensions [17–19].

Simulation method.— The hydrodynamic fields are calculated on nodes inside the cells of a fixed Cartesian grid. Due to this discrete nature of the LBM, one needs to discretize the unit of length (smallest particle radius a_{\min}) into the lattice unit $\Delta x = 0.2a_{\min}$ for the hydrodynamic fields calculations. To simulate the free surface of the fluid, it is necessary to introduce interface nodes between the fluid and gas nodes, where we calculate the fluid density in a single cell m_f and liquid fraction λ [17–19]. To maintain a smooth surface and conserve m_f , the surplus of m_f during time evolution is distributed equally among interface nodes. The detailed explanation on how to calculate the hydrodynamic fields, and the rules of evolution equation for m_f are written in the Supplemental Materials.

The motion and the torque of the particle i are given by $m_i \frac{d\mathbf{u}_i}{dt} = \mathbf{F}_i^c + \mathbf{F}_i^h + \mathbf{F}_i^r + \mathbf{F}_i^g$ and $I_i \frac{d\boldsymbol{\omega}_i}{dt} = \mathbf{T}_i^c + \mathbf{T}_i^h$, respectively. Here, \mathbf{u}_i , $\boldsymbol{\omega}_i$, m_i , and I_i are the translational velocity, angular velocity, mass, and the moment of inertia of particle i , respectively. $\mathbf{F}_i^g = -m_i g \hat{\mathbf{z}}$ is the gravitational force acting on the suspended particles, where g is the gravitational acceleration and $\hat{\mathbf{z}}$ is the

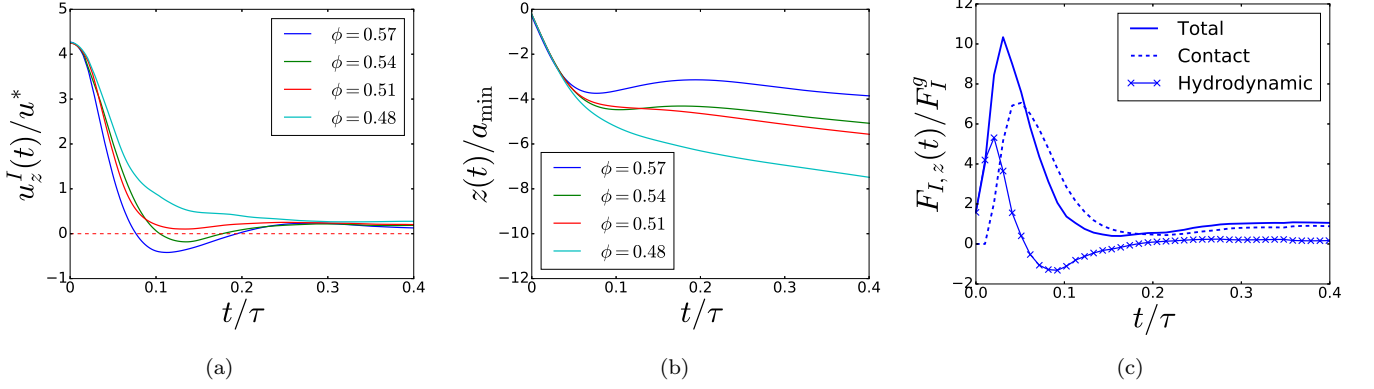


FIG. 1. (a) Plots of impactor speed in z -direction $u_z^I(t)/u^*$ against time for various volume fraction ϕ . (b) Plots of the impactor height $z(t)/a_{\min}$ against time for various volume fraction ϕ . (c) Plots of the z -component of exerted force on the impactor $F_{I,z}$ scaled by gravitational force F_I^g (solid line) and its contributions, contact (dashed line), and hydrodynamics (cross symbols), for $\phi = 0.57$ and $u_{0,z}^I/u^* = 4.2$ (blue lines in (a) and (b)).

unit vector in vertical direction. The ingredients of our model are similar to the lubrication friction discrete element method (LF-DEM) [9, 10]. Nevertheless, our LBM considers both the short and long-range parts for the hydrodynamic force \mathbf{F}_i^h and torque \mathbf{T}_i^h [12, 20] (See Supplementary Materials for the details), though LF-DEM contains only the short-range force. The contact force and torque \mathbf{F}_{ij}^c and \mathbf{T}_{ij}^c are computed using the linear-dashpot model with Coulomb friction rules and friction coefficient μ [21]. We mainly use $\mu = 1$ for our simulations but will discuss μ -dependence later. Finally, we also introduce the pairwise double-layer electrostatic repulsive force \mathbf{F}_{ij}^r to prevent particles from clustering [10, 12].

About 600 suspended particles (bidisperse particles with bidispersity ratio $a_{\max} = 1.2a_{\min}$ where the radii of the large and small particles are a_{\max} and a_{\min} , respectively) are confined in a rectangular box ($W \times D \times H$) where we adopt the width $W = D = 24a_{\min}$, and height $H = 12a_{\min}$. We adopt the reflection rule as the boundary condition on the walls. The impactor is a solid spherical object with radius $a_I = 3a_{\min}$, and density $\rho_I = 4\rho_f$, where ρ_f is the density of suspended particles and solvent. The impactor also obeys Newton's equation of motion with total force $\mathbf{F}_I = \mathbf{F}_I^h + \mathbf{F}_I^c + \mathbf{F}_I^g$, and total torque $\mathbf{T}_I = \mathbf{T}_I^h + \mathbf{T}_I^c$, where $\mathbf{F}_I^g = -m_I g \hat{\mathbf{z}}$ is the gravitational force acting on the impactor with mass m_I . The contact force \mathbf{F}_I^c is calculated with similar manner as the suspended particles, while the hydrodynamic force \mathbf{F}_I^h is calculated with the bounce-back rules [14, 15]. In order to maintain numerical stability, we ignore the lubrication torque on the impactor (regarding the surface of impactor as planar surface) as exemplified in Ref. [20]. However, the torque from contact are still considered. The impactor is released from various height H_0 that corresponds to the impact velocity as $u_0^I = \sqrt{2gH_0}$,

which also specifies the unit of time in our simulation $\tau = \sqrt{a_{\min}/2g}$, unit velocity $u^* = \sqrt{2ga_{\min}}$, unit of force $F_0 = \frac{4}{3}\pi\rho_f a_{\min}^3 g$, and unit of stress $\sigma_0 = F_0/a_{\min}^2$.

Impact induced hardening.— First, we plot the impactor speeds $u_z^I(t)/u^*$ as functions of time for various volume fractions ϕ in Fig. 1(a), where we set the time $t = 0$ and height $z = 0$ at the impact moment. The plots for the heights (z/a_{\min}) of impactors can be seen in Fig. 1(b). One can observe bouncing of the impactor ($u_z^I(t)/u^* < 0$) for the volume fraction $\phi \geq 0.54$ as in a free-falling projectile experiment [6] due to the hardening of the suspension shortly after the impact. After the rebound, the suspension becomes soft, and the impactor sinks, where the sinking speed is a constant. Note that the critical ϕ for rebounds is a little higher than that in the experiment [6] since our simulations ignore the rolling friction (See Ref. [22]). When the impactor bounces, one can observe a peak in $F_{I,z}$ which is z -component of \mathbf{F}_I (Fig. 1(c)), where we plot the total force exerted on the impactor for $\phi = 0.57$ and $u_{0,z}^I/u^* = 4.2$ (the blue lines in Figs. 1(a) and 1(b)). Furthermore, we can see a visible peak in the contact force, which proceeds by weak hydrodynamic contribution. The separation between those peaks are so short that they form a single peak in the total force. This behavior is similar to the observation in an experiment of rod impactor [1], where they observe two peaks in the impactor acceleration for deep suspensions. In the contrary for the shallower suspension, in which rebound takes place, the separation between those two peaks is not detectable. Moreover, they also observed the second peak when the impact force is transmitted to the boundary [1]. Here, the peak of the contact forces between particles in our simulation corresponds to their second peak. This indicates that the hardening takes place when the network of the contact force is percolated from the impactor to the boundaries. [23]

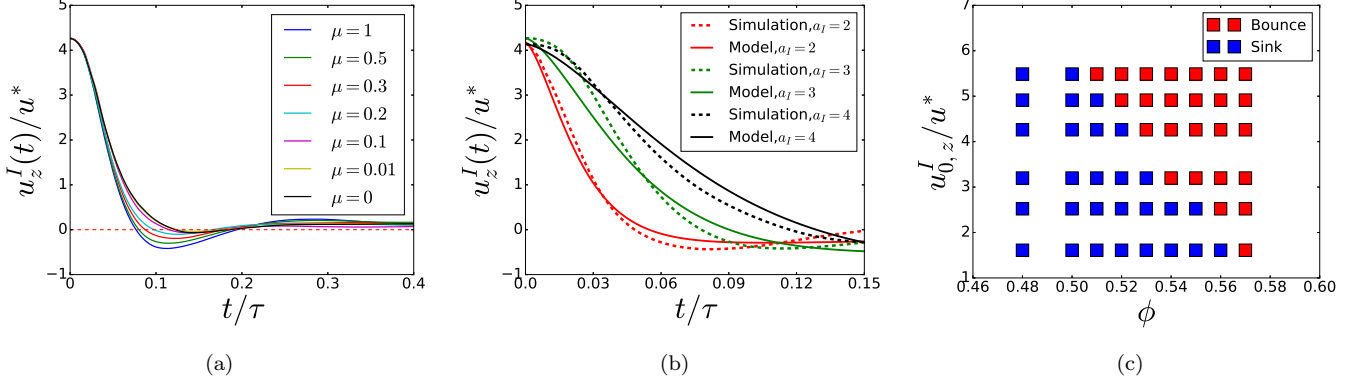


FIG. 2. (a) Plots of the speeds of impactor in z -direction $u_z^I(t)/u^*$ against time for $\phi = 0.57$ and various friction coefficients μ . (b) Plots of the speeds of impactors in z -direction $u_z^I(t)/u^*$ against time and the solution of Eq. (1) for $\phi = 0.57$, with fitting parameters $A = 2.14 \times 10^5 m_0/(a_{\min} \tau^2)$ and $B = 5.65 \times 10^4 m_0/(a_{\min} \tau)$ for all a_I , where $m_0 = 4\pi a_{\min}^3 \rho_f/3$. (c) Phase diagram for the bouncing or sink on the plane of the control parameters volume fraction ϕ and the the impact speed $u_{0,z}^I$.

To clarify the importance of the contact friction further, we simulate various friction coefficient μ to see its dependencies. In Fig. 2(a), one can observe that the bouncing motion is weakened as μ decreases. This stands as the second proof that frictional contacts between particles are necessary to induce the resistance that makes the impactor rebounds. This μ -dependence is analogous to that for DST in dense suspensions under steady shear [8–12] and for impact in dry granular materials [24].

Figure 2(b) shows a clear dependence on the impactor radius a_I . Therefore, we try to characterize the elasticity of suspensions by the viscoelastic Hertzian law for contact [25, 26]. The equation motion for the deformation h for the Hertzian contact is written as

$$m_I \frac{d^2 h}{dt^2} = -A\sqrt{a_I} h^{\frac{3}{2}} - B\sqrt{a_I} h^{\frac{1}{2}} \frac{dh}{dt}, \quad (1)$$

where A and B are fitting parameters which correspond to the elastic modulus and viscosity, respectively. In Fig. 2(b), we plot the simulation results alongside with the solutions of Eq. (1). Although there are gaps (i) to identify the depth with the deformation and (ii) to ignore hydrodynamic and gravity effects acting on the impactor, one can see that they agree in shortly after the impact when the rebound takes place and deviate afterwards. In other words, this picture is only valid when h is small. Therefore, this does not contradict the observation in Ref. [3], where the suspensions have plastic response under impact since their impactor penetrates to the bottom boundary (large h).

The observations on possible running on suspensions are successfully mimicked through our simulations, where we also observe that the impact-induced hardening depends on the impact speed $u_{0,z}^I$, as shown in the phase diagram in Fig. 2(c). Although it is not observed clearly in Ref. [6], the speed dependence also exists in the simulation of rotating wheel on top of the suspensions [13].

Note that the highest $\phi_{\max} = 0.57$ in our simulation is still below the frictional ($\mu = 1$) jamming fraction $\phi_J^{\mu=1} \approx 0.585$ for $\mu = 1$ [10], whereas the bouncing takes place for $\phi_{\min} \leq \phi \leq \phi_{\max}$, with lowest observed bouncing volume fraction $\phi_{\min} = 0.51$. This range reminds us of the observed volume fractions for both CST and DST under simple shear in numerical simulations [9, 10, 12]. However, one should recognize that two processes are completely different since the impact-induced hardening is a heterogeneous and transient process, while the shear thickening is homogeneous in steady states. [27]

To understand the stress response of the suspension, we visualize the normal component of the stress on each suspended particle σ_{zz} right after the impact, sliced in the middle of the container as shown in Fig. 3(a). Here we can see the existence of a localized region with distinctively high normal stress value, from the impactor to the bottom boundary. On the contrary, we observe a uniformly weak magnitude of the shear stress (See Supplemental Materials). Note that this localized response of the normal stress is also a clear distinction between the impact and shear thickening phenomena. To see the origin of this mechanism in the microscopic level, we visualize the magnitude of the normal contact forces between particles scaled by the gravitational force $|\mathbf{F}_{ij}^{c,n}|/F_0$ right after the impact in Fig. 3(b). The percolating force chains span from the impactor to the bottom boundary. The regions of large σ_{zz} and the force chains correspond to the dynamically jammed region in Fig. 3(a) and Refs. [1, 3–5], where we also observe a spanning region of high particle displacement Δz (see Supplemental Materials). As indicated in Refs. [2, 3, 13], the propagation speed of the jamming front depends on the impact speed. One can imagine that the sudden change of stress right after the impactor stops makes the suspension softs and let the impactor sinks.

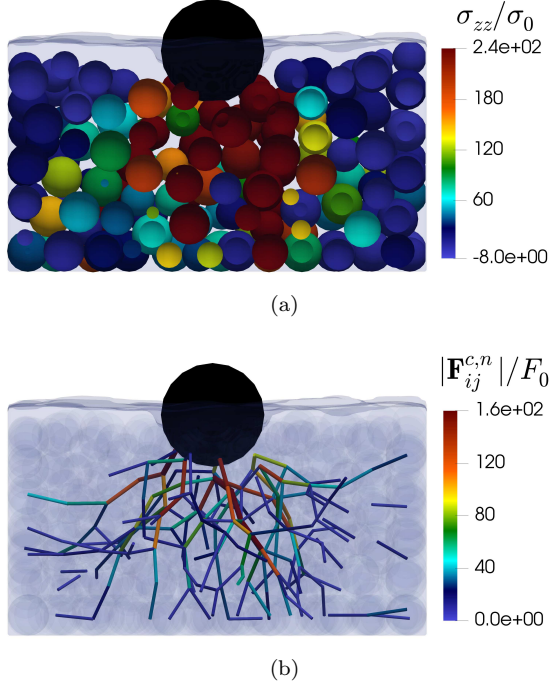


FIG. 3. (a) Snapshot of the particles, sliced in the middle of the box for $\phi = 0.57$ and $u_{0,z}^I/u^* = 4.2$, shortly after the impact, where the color represents the dimensionless normal stress σ_{zz}/σ_0 . (b) Snapshot of the force chains made by normal contact forces scaled by the gravitational force $|\mathbf{F}_{ij}^{c,n}|/F_0$ for $\phi = 0.57$ and $u_{0,z}^I/u^* = 4.2$, shortly after the impact, where the color and line thickness represent the magnitude of the force.

Persistent homology.— To elucidate the important feature of the force chains, we try to grasp its topological structure by using the persistent homology [28]. In addition to successful distinction of the liquid, amorphous, and crystalline states of silica glass [29], the persistent homology allows us to quantify the topological structure of the force chains in granular materials [30, 31], and in dense suspensions under simple shear [32]. Since no visible loops or higher dimensional structures are observed from the force chains in Fig. 3(b), the topological structure we consider is only the connected component represented by the zeroth Betti numbers β_0 . The idea of the persistent homology is to filter the force chains by increasing threshold θ_f , where a link in the force chains appears if $|\mathbf{F}_{ij}^{c,n}|/F_0 \leq \theta_f$. We regard this as the birth of a connected component. As the threshold is further increased, the structure grows in size as additional contacts are added. When multiple connected components merge, the structure that is born later in the filtration (which has higher birth θ_f) dies. We record the birth θ_f as $\theta_{f,b}$ and death θ_f as $\theta_{f,d}$. This rule also ensures $\theta_{f,d} > \theta_{f,b}$. The program to filter the chains is available in public domain [33, 34]. Note that in Refs. [30–32], $\theta_{f,b}$ is always larger than $\theta_{f,d}$, since they adopt the filtration

by reducing the threshold. We plot $\theta_{f,d}$ against $\theta_{f,b}$ for all connected components that appears in Fig. 3(b) in the persistence diagram (Fig. 4(a)). The time evolution of the force chains and persistence diagram can also be seen in the Supplemental movie [35]. Shortly after the impact, we observe more points far from the diagonal, which represent the connected components to persist through the increment of force threshold with the lifespan $(\theta_{f,d} - \theta_{f,b})$. Due to the continuity of the force among the suspensions, the only possible mechanism for the existence of long lifespan for connected components is by forming a long chain. One can regard this as a quantitative proof of the existence of percolated force chains. The component with $\theta_{f,d} = -1$ is the component that has infinite persistence, i.e. never dies until the filtration ends. The persistent homology ignores the effect of such contact forces.

The total persistence for the connected components TP_0 is the sum of all lifespan in the persistence diagram

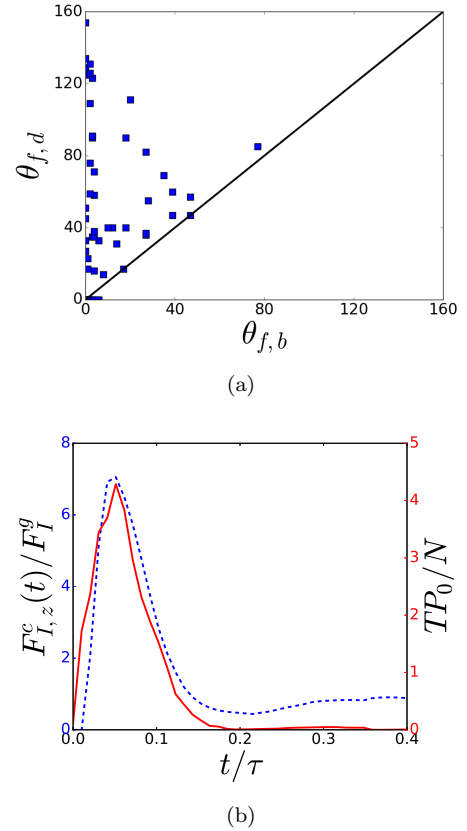


FIG. 4. (a) Persistence diagram of the connected components for $\phi = 0.57$ and $u_{0,z}^I/u^* = 4.2$, shortly after the impact. (b) Plot of the total persistence for the connected components TP_0 scaled by the number of suspended particles N against time for $\phi = 0.57$ and $u_{0,z}^I/u^* = 4.2$ (red lines). Plot of the corresponding contact force on the impactor in the z -direction $F_{I,z}^c$ (dashed blue lines).

PD_0

$$TP_0 = \sum_{(\theta_{f,d}, \theta_{f,b}) \in PD_0} (\theta_{f,d} - \theta_{f,b}). \quad (2)$$

This allows us to describe the persistence diagram by a single number as a cost of information loss. Higher TP_0 means merging of longer connected components (percolated force chains), while $TP_0 = 0$ means no merging of the connected components. Note that we ignore the components with infinite persistence since we are only interested in the extraction of the structural information. We plot TP_0 scaled by the number of suspended particles N against time in Fig. 4(b). It is remarkable that TP_0 reaches its peak at the same time as the corresponding contact force and the shape of TP_0 is similar to that of the contact force. When the suspension becomes soft and the impactor sinks, we found $TP_0 = 0$, even though there are still contributions from the contact forces. These contributions come from the singular (not percolated) force chains near the impactor. In other words, the peak of the contact force that induces the hardening of the suspension comes from their structure, i.e. the existence of percolated force chains. Our results support the argument in Refs. [1, 3–6] that indicate the importance of the boundaries to sustain percolated force chains. Meanwhile, for sheared suspensions, the total persistence for loops is more significant as it behaves similarly to the viscosity [32]. This distinction exists because the force chains are more structured and uniformly distributed for sheared suspensions than those in the impact case.

Conclusions and outlook.— We have reproduced the impact-induced hardening and the dynamically jammed region in dense suspensions through particles-based simulations. Remarkably, with the aid of the persistence homology, one can confirm the existence of a percolated force chains when impact-induced hardening takes place.

Due to the limitation of our computational resources, we have not analyzed the dependence on the system size as well as dependences on H and W . A sinking heavy intruder in dense suspensions shows a distinct behavior, as it oscillates and has a stop-go cycle near the bottom [36]. Although our preliminary simulation reproduces such a process, we avoid including the analysis of it because the physics behind it is different from that explained in this Letter. Our simulation method and analysis can also be applied to the impactor rebound within the view of the jamming transition as in Ref. [37], where they unified the shear jamming and the DST pictures. Nevertheless, we avoid such discussions in this Letter in which one needs to apply shear to the suspensions before dropping the impactor and will induce a completely different response. A recent paper observe the existence of a universal scaling law for impacts in dry granular media [38]. It would be interesting to analyze whether such a scaling law exists in the impact on suspensions.

One of the authors (HH) thanks H. Katsuragi for his insights in the early stage of this research. One of the authors (P) expresses his gratitude to A. Leonardi for sharing his lattice Boltzmann code. The authors thank M. Otsuki, R. Seto, T. Nakamura, and T. Yamaguchi for their useful comments and fruitful discussions. All numerical calculations were carried out at the Yukawa Institute for Theoretical Physics (YITP) Computer Facilities, Kyoto University, Japan.

-
- [1] S. R. Waitukaitis and H. M. Jaeger, Impact-activated solidification of dense suspensions via dynamic jamming fronts, *Nature* **487**, 205 (2012).
 - [2] I. R. Peters and H. M. Jaeger, Quasi-2d dynamic jamming in cornstarch suspensions: visualization and force measurements, *Soft Matter* **10**, 6564 (2014).
 - [3] R. Maharjan, S. Mukhopadhyay, B. Allen, T. Storz, and E. Brown, Constitutive relation for the system-spanning dynamically jammed region in response to impact of cornstarch and water suspensions, *Phys. Rev. E* **97**, 052602 (2018).
 - [4] B. Allen, B. Sokol, S. Mukhopadhyay, R. Maharjan, and E. Brown, System-spanning dynamically jammed region in response to impact of cornstarch and water suspensions, *Phys. Rev. E* **97**, 052603 (2018).
 - [5] S. Mukhopadhyay, B. Allen, and E. Brown, Testing constitutive relations by running and walking on cornstarch and water suspensions, *Phys. Rev. E* **97**, 052604 (2018).
 - [6] K. Egawa and H. Katsuragi, Bouncing of a projectile impacting a dense potato-starch suspension layer, *Phys. Fluids* **31**, 053304 (2019).
 - [7] A. H. Clark, A. J. Petersen, L. Kondic, and R. P. Behringer, Nonlinear force propagation during granular impact, *Phys. Rev. Lett.* **114**, 144502 (2015).
 - [8] M. Otsuki and H. Hayakawa, Critical scaling near jamming transition for frictional granular particles, *Phys. Rev. E* **83**, 051301 (2011).
 - [9] R. Seto, R. Mari, J. F. Morris, and M. M. Denn, Discontinuous shear thickening of frictional hard-sphere suspensions, *Phys. Rev. Lett.* **111**, 218301 (2013).
 - [10] R. Mari and R. Seto, Shear thickening, frictionless and frictional rheologies in non-brownian suspensions, *J. Rheol* **58**, 1693 (2014).
 - [11] J. E. Thomas, K. Ramola, A. Singh, R. Mari, J. F. Morris, and B. Chakraborty, Microscopic origin of frictional rheology in dense suspensions: Correlations in force space, *Phys. Rev. Lett.* **121**, 128002 (2018).
 - [12] Pradipto and H. Hayakawa, Simulation of dense non-brownian suspensions with the lattice boltzmann method: shear jammed and fragile states, *Soft Matter* **16**, 945 (2020).
 - [13] A. S. Baumgarten and K. Kamrin, A general constitutive model for dense, fine-particle suspensions validated in many geometries, *Proc. Natl. Acad. Sci. U. S. A.* **116**, 20828 (2019).
 - [14] A. J. C. Ladd, Numerical simulations of particulate suspensions via a discretized boltzmann equation. part 1. theoretical foundation, *J. Fluid Mech* **271**, 285 (1994).
 - [15] A. J. C. Ladd, Numerical simulations of particulate sus-

- pensions via a discretized boltzmann equation. part 2. numerical simulations, *J. Fluid Mech* **271**, 311 (1994).
- [16] S. Succi, *The lattice Boltzmann equation: for fluid dynamics and beyond* (Oxford University Press, 2001).
 - [17] O. Švec, J. Skocek, H. Stang, M. R. Geiker, and N. Rous-
sel, Free surface flow of a suspension of rigid particles in
a non-newtonian fluid: A lattice boltzmann approach, *J.*
Non-Newton. Fluid. **179-180**, 32 (2012).
 - [18] A. Leonardi, F. K. Wittel, M. Mendoza, and H. J. Her-
mann, Coupled dem-lbm method for the free-surface sim-
ulation of heterogeneous suspensions, *Comp. Part. Mech.*
1, 3 (2014).
 - [19] A. Leonardi, M. Cabrera, F. K. Wittel, R. Kaitna,
M. Mendoza, W. Wu, and H. J. Herrmann, Granular-
front formation in free-surface flow of concentrated sus-
pensions, *Phys. Rev. E* **92**, 052204 (2015).
 - [20] N. Q. Nguyen and A. J. C. Ladd, Lubrication corrections
for lattice-boltzmann simulations of particle suspensions,
Phys. Rev. E **66**, 046708 (2002).
 - [21] S. Luding, Cohesive, frictional powders: contact models
for tension, *Granul. Matter.* **10**, 235 (2008).
 - [22] A. Singh, C. Ness, R. Seto, J. J. de Pablo, and H. M.
Jaeger, arXiv:2002.10996 (2020).
 - [23] It should be noted that there is no distinct peak in $F_{I,z}$
when the impactor does not bounce (see Supplemental
Materials).
 - [24] L. Kondic, X. Fang, W. Losert, C. S. O'Hern, and R. P.
Behringer, Microstructure evolution during impact on
granular matter, *Phys. Rev. E* **85**, 011305 (2012).
 - [25] G. Kuwabara and K. Kono, Restitution coefficient in a
collision between two spheres, *Jpn. J. Appl. Phys.* **26**,
1230 (1987).
 - [26] N. V. Brilliantov, F. Spahn, J.-M. Hertzsch, and
T. Poschel, Model for collisions in granular gases, *Phys.*
Rev. E **53**, 5382 (1996).
 - [27] There is another difference between two processes as
mentioned in Supplemental Materials in which the shear
stress is as large as the normal stress in DST while the
shear stress is much smaller than the normal stress in
impact processes.
 - [28] G. Carlsson, Topology and data, *Bull. Am. Math. Soc.*
46, 255 (2009).
 - [29] Y. Hiraoka, T. Nakamura, A. Hirata, E. G. Escobar,
K. Matsue, and Y. Nishiura, Hierarchical structures of
amorphous solids characterized by persistent homology,
Proc. Natl. Acad. Sci. U. S. A. **113**, 7035 (2016).
 - [30] M. Kramar, A. Goulet, L. Kondic, and K. Mischaikow,
Evolution of force networks in dense particulate media,
Phys. Rev. E **90**, 052203 (2014).
 - [31] T. Takahashi, A. H. Clark, T. Majmudar, and L. Kondic,
Granular response to impact: Topology of the force net-
works, *Phys. Rev. E* **97**, 012906 (2018).
 - [32] M. Gameiro, A. Singh, L. Kondic, K. Mischaikow, and
J. F. Morris, Interaction network analysis in shear thicken-
ing suspensions, *Phys. Rev. Fluids* **5**, 034307 (2020).
 - [33] K. Mischaikow and V. Nanda, Morse theory for filtra-
tions and efficient computation of persistent homology,
Discrete. Comput. Geom **50**, 330 (2013).
 - [34] V. Nanda, Perseus, the persistent homology software,
<http://people.maths.ox.ac.uk/nanda/perseus/>.
 - [35] Supplemental movies for force chains and persistence diagram.
 - [36] S. von Kann, J. H. Snoeijer, D. Lohse, and D. van der
Meer, Nonmonotonic settling of a sphere in a cornstarch
suspension, *Phys. Rev. E* **84**, 060401 (2011).
 - [37] I. R. Peters, S. Majumdar, and H. M. Jaeger, Direct
observation of dynamic shear jamming in dense suspen-
sions, *Nature* **532**, 214 (2016).
 - [38] N. Krizou and A. H. Clark, Power-law scaling of early-
stage forces during granular impact, *Phys. Rev. Lett.*
124, 178002 (2020).

Supplemental Material for "Impact-Induced Hardening on Dense Frictional Suspensions"

Pradipto and Hisao Hayakawa

*Yukawa Institute for Theoretical Physics, Kyoto University,
Kitashirakawaoiwake-cho, Sakyo-ku, Kyoto 606-8502, Japan*

(Dated: May 7, 2020)

I. LATTICE BOLTZMANN METHOD FOR SUSPENSIONS WITH FREE SURFACE

A. Review on the lattice Boltzmann method

In this section, we review the essential parts of the lattice Boltzmann method (LBM) based on Refs. [S1–S6]. Due to the discrete nature of the LBM, one needs to discretize the unit of length into the lattice unit Δx . In LBM, the hydrodynamic fields (density ρ_f and velocity \mathbf{u}_f) are calculated on nodes \mathbf{r} inside cells of a fixed Cartesian grid as

$$\rho_f(\mathbf{r}) = \sum_{\mathbf{q}} f_{\mathbf{q}}(\mathbf{r}) \Delta c^3, \quad \rho_f \mathbf{u}_f(\mathbf{r}) = \sum_{\mathbf{q}} f_{\mathbf{q}} \mathbf{c}_{\mathbf{q}}(\mathbf{r}) \Delta c^3, \quad (\text{S1})$$

where $\mathbf{c}_{\mathbf{q}}$ is the lattice velocity of the direction \mathbf{q} , and Δc^3 is the volume element in the velocity space with $\Delta c = \Delta x / \Delta t$. $f_{\mathbf{q}}(\mathbf{r})$ is the abbreviation of $f_{\mathbf{q}}(\mathbf{r}, t)$ which is the discrete distribution function and has the dimension of mass density. The evolution equation for $f_{\mathbf{q}}(\mathbf{r}, \mathbf{c}_{\mathbf{q}})$ is

$$f_{\mathbf{q}}(\mathbf{r} + \mathbf{c}_{\mathbf{q}} \Delta t, t + \Delta t) = f_{\mathbf{q}}(\mathbf{r}, t) + \Omega_{\mathbf{q},c} + \Delta t \Omega_{\mathbf{q},f}, \quad (\text{S2})$$

where $\Omega_{\mathbf{q},c}$ is the collision operator and $\Omega_{\mathbf{q},f}$ is an additional operator if a volumetric force density $\tilde{\mathbf{f}}$ acts on the system. We use the Bhatnagar-Gross-Krook approximation for the collision operator [S7], which relaxes the system to the equilibrium state $f_{\mathbf{q}}^{\text{eq}}$ as

$$\Omega_{\mathbf{q},c} = \frac{f_{\mathbf{q}}^{\text{eq}} - f_{\mathbf{q}}}{\tau_r}, \quad (\text{S3})$$

where τ_r is the relaxation time relating to the kinematic viscosity ν as $\tau_r = \Delta t(1/2 + \nu/c_s^2)$, with c_s is the lattice sound speed, $c_s = \sqrt{\Delta c^2/3}$. The equilibrium distribution function $f_{\mathbf{q}}^{\text{eq}} = f_{\mathbf{q}}^{\text{eq}}(\rho_f, \mathbf{u}_f)$ is calculated as

$$f_{\mathbf{q}}^{\text{eq}}(\rho_f, \mathbf{u}_f) \Delta c^3 = w_{\mathbf{q}} \rho_f \left[1 + \frac{\mathbf{c}_{\mathbf{q}} \cdot \mathbf{u}_f}{c_s^2} + \frac{\mathbf{u}_f \mathbf{u}_f : \mathbf{c}_{\mathbf{q}} \mathbf{c}_{\mathbf{q}} - c_s^2 \mathbf{I}}{2c_s^4} \right] \quad (\text{S4})$$

where $w_{\mathbf{q}}$ is the lattice weight that depends on the configurations. For $\Omega_{\mathbf{q},f}$, we employ [S8]

$$\Omega_{\mathbf{q},f} \Delta c^3 = w_{\mathbf{q}} \left(1 - \frac{\Delta t}{2\tau_r} \right) \left[\frac{(\mathbf{c}_{\mathbf{q}} - \mathbf{u}_f)}{c_s^2} + \frac{(\mathbf{c}_{\mathbf{q}} \cdot \mathbf{u}_f)}{c_s^4} \mathbf{c}_{\mathbf{q}} \right] \cdot \tilde{\mathbf{f}}. \quad (\text{S5})$$

As a result, the macroscopic velocity is changed so the second term in Eq. (S1) becomes

$$\rho_f \mathbf{u}_f(\mathbf{r}) = \sum_{\mathbf{q}} f_{\mathbf{q}} \mathbf{c}_{\mathbf{q}}(\mathbf{r}) \Delta c^3 + \frac{\Delta t \tilde{\mathbf{f}}(\mathbf{r})}{2}. \quad (\text{S6})$$

B. Handling the free surface of the fluid

To simulate the free surface, we need to implement the mass tracking algorithm [S9–S11]. First, we assign a type of nodes such as the fluid, interface, or gas node for each node, where the interface node exists between the fluid and gas nodes as in Fig. S1. Note that Eqs. (S1) and (S2) are only used in the fluid and interface nodes.

A gas node represents the cell which is not occupied by the fluid, hence $f_{\mathbf{q}} = 0$. An interface node expresses the interface between fluid and gas, where the streaming and collision of $f_{\mathbf{q}}$ exist as in fluid nodes. Here, we introduce a variable m_f , which represents the density of the fluid in a single cell, to track the evolution of the surface. The interface node turns into a fluid node if $m_f \geq \rho_f^*$ or into a gas node if $m_f \leq 0$, where ρ_f^* is the unit density of the fluid. Therefore, the state of each node is characterized by the liquid fraction λ :

$$\begin{cases} \lambda = 1 & \text{if the node is liquid} \\ 0 < \lambda < 1 & \text{if the node is interface,} \\ \lambda = 0 & \text{if the node is gas,} \end{cases}$$

where $m_f = \lambda \rho_f$. The evolution of the m_f is determined by the balance between the populations streaming into the node $f_{\mathbf{q}'}(\mathbf{r} + \mathbf{c}_{\mathbf{q}'} \Delta t, t)$ ($\mathbf{q}' = -\mathbf{q}$) and out of the node $f_{\mathbf{q}}(\mathbf{r}, t)$

$$m_f(t + \Delta t) = \Delta t \sum_{\mathbf{q}} \alpha_{\mathbf{q}} (f_{\mathbf{q}'}(\mathbf{r} + \mathbf{c}_{\mathbf{q}'} \Delta t, t) - f_{\mathbf{q}}(\mathbf{r}, t)) \Delta c^3 + m_f(t), \quad (\text{S7})$$

where $\alpha_{\mathbf{q}}$ is a function of λ of the neighboring node (located at $\mathbf{r} + \mathbf{c}_{\mathbf{q}'} \Delta t$).

$$\alpha_{\mathbf{q}} = \begin{cases} \frac{1}{2}[\lambda(\mathbf{r}, t) + \lambda(\mathbf{r} + \mathbf{c}_{\mathbf{q}'}\Delta t, t)] & \text{if } f_{\mathbf{q}'}(\mathbf{r} + \mathbf{c}_{\mathbf{q}'}\Delta t, t) \text{ streams from an interface node,} \\ 1 & \text{if } f_{\mathbf{q}'}(\mathbf{r} + \mathbf{c}_{\mathbf{q}'}\Delta t, t) \text{ streams from a fluid node,} \\ 0 & \text{if } f_{\mathbf{q}'}(\mathbf{r} + \mathbf{c}_{\mathbf{q}'}\Delta t, t) \text{ streams from a gas node.} \end{cases} \quad (\text{S8})$$

When an interface node turns into a fluid node, the neighboring gas nodes turn into interface nodes. When an interface node turns into a gas node, the neighboring fluid nodes turn into interface nodes. Although the density in a continuum model must be conserved, the discrete model can contain small loss or gain of m_f . The surplus (or shortfall including the possibility of negative density) of m_f is then computed at every time step and is corrected to satisfy the conservation among all interface nodes.

Fixed-pressure boundary condition. As stated before, LBM equations are solved only in the liquid and interface nodes. This creates a problem in the implementation since the population streaming to the interface nodes from gas nodes which is necessary in Eq. (S2) is not well-defined. Assuming that the gas node is always in equilibrium and has the same velocity of the interface node \mathbf{u}_f^{in} and a constant atmospheric density $\rho_a < \rho_f$, the incoming distribution function (first term on the right hand side of Eq. (S2)) is replaced by the equilibrium distribution function with \mathbf{u}_f^{in} and ρ_a [S5],

$$f_{\mathbf{q}}(\mathbf{r}, t) \rightarrow f_{\mathbf{q}}^{\text{eq}}(\mathbf{u}_f^{\text{in}}, \rho_a). \quad (\text{S9})$$

This is analogous to applying a fixed-pressure boundary condition at the interface, and local symmetry conditions for the velocity.

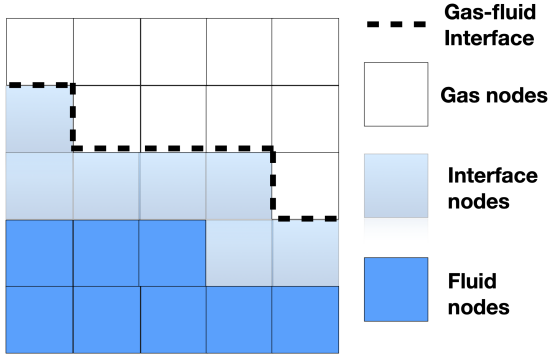


FIG. S1. Illustration of the the division of the lattice nodes into fluid, interface and gas nodes.

C. Solid boundaries and the fluid-particle coupling

We implement two coupling schemes to handle solid boundaries within our simulations. We use the bounce-back rules for no-slip boundary condition on walls and the

surface of the impactor, while we use the direct forcing scheme for suspended particles. *The bounce-back rule* simply states that whenever a population is streaming towards a wall, this population is reflected and bounced back in the opposite direction. This rule can be expressed as

$$f_{\mathbf{q}'}(\mathbf{r}, t + \Delta t) = f_{\mathbf{q}}(\mathbf{r}, t), \quad (\text{S10})$$

in LBM notation. If the wall is moving, the reflection has to take into account the momentum transfer by an additional term [S3, S4]

$$\{f_{\mathbf{q}}(\mathbf{r}, t) - f_{\mathbf{q}'}(\mathbf{r}, t + \Delta t)\} \Delta c^3 = \left(\frac{2w_{\mathbf{q}}\rho_f \mathbf{u}_w \cdot \mathbf{c}_{\mathbf{q}}}{c_s^2} \right), \quad (\text{S11})$$

where \mathbf{u}_w is the wall velocity. Here, \mathbf{u}_w is calculated as

$$\mathbf{u}_w(\mathbf{r}) = \mathbf{u}^I + (\mathbf{r} - \mathbf{R}^I) \times \boldsymbol{\omega}^I, \quad (\text{S12})$$

where \mathbf{u}^I , $\boldsymbol{\omega}^I$ are the translational velocity and the angular velocity on the surface of the impactor, respectively, and \mathbf{R}^I denotes the center of mass of the impactor. The momentum exchange described in Eq. (S11) results in a force on each node on the impactor surface $\tilde{\mathbf{F}}(\mathbf{r})$ as

$$\tilde{\mathbf{F}}(\mathbf{r}) = \frac{\Delta x^3}{\Delta t} \left(2f_{\mathbf{q}}(\mathbf{r}, t) \Delta c^3 - \frac{2w_{\mathbf{q}}\rho_f \mathbf{u}_w \cdot \mathbf{c}_{\mathbf{q}}}{c_s^2} \right) \mathbf{c}_{\mathbf{q}}. \quad (\text{S13})$$

The hydrodynamic force on the impactor \mathbf{F}_I^h is the sum of the forces for all nodes in the surface as $\mathbf{F}_I^h =$

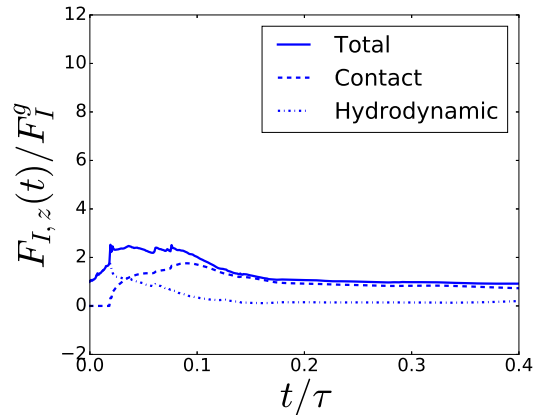


FIG. S2. Plots the z -component of exerted force on the impactor $F_{I,z}$ (solid line) scaled by gravitational force $F_I^g = m_I g \hat{\mathbf{z}}$ for $\phi = 0.54$ and $u_{0,z}^I/u^* = 1.61$ and its contributions: contact (dashed line), and hydrodynamic forces (dot-dashed line), respectively.

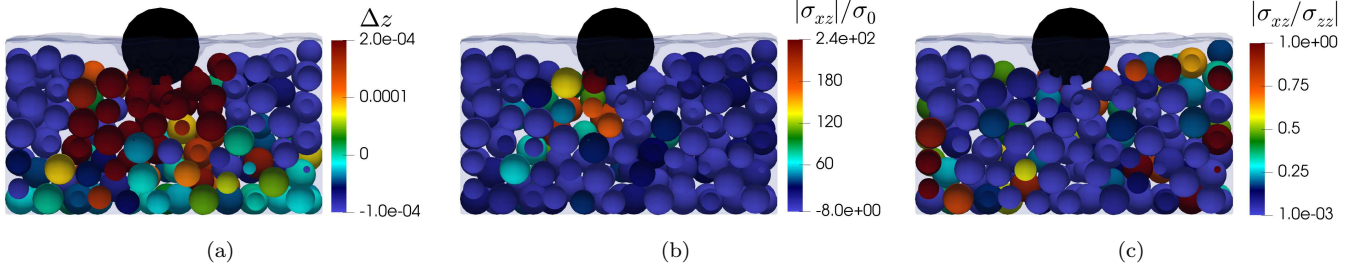


FIG. S3. Snapshots of the particles, sliced in the middle of the box for $\phi = 0.57$ and $u_{0,z}^I/u^* = 4.2$, shortly after the impact, where the color represents: (a) the normal displacement Δz , (b) Dimensionless shear stress σ_{xz}/σ_0 , and (c) the absolute ratio between the shear and normal stress $|\sigma_{xz}/\sigma_{zz}|$.

$\sum_{\mathbf{r} \in \text{surface}} \tilde{\mathbf{F}}(\mathbf{r})$, while $\mathbf{T}_l^h = \sum_{\mathbf{r} \in \text{surface}} (\mathbf{r} - \mathbf{R}^I) \times \tilde{\mathbf{F}}(\mathbf{r})$ is the hydrodynamic torque.

Direct forcing. By using the immersed boundary method, we calculate the hydrodynamic force through an additional discretization of particles into a set of segments \mathbf{r}_{cell} . These particle segments are related to the fluid simulation by an interpolating function [S12]. We implement the simplified version [S5, S11], where the segments correspond to the lattice nodes of the LBM $\mathbf{r}_{\text{cell}} = \mathbf{r}$. Since the volume of a cubic cell is unity, the hydrodynamic force on each cell $\tilde{\mathbf{F}}_{\text{cell}}(\mathbf{r})$ can be computed directly from the velocity differences

$$\tilde{\mathbf{F}}_{\text{cell}}(\mathbf{r}) = \frac{\Delta x^3}{\Delta t} \rho_f(\mathbf{r}) [\mathbf{u}_f(\mathbf{r}) - \mathbf{u}_{\text{cell}}(\mathbf{r})], \quad (\text{S14})$$

where \mathbf{u}_{cell} is the velocity of the particle cell

$$\mathbf{u}_{\text{cell}}(\mathbf{r}) = \mathbf{u} + (\mathbf{r} - \mathbf{R}) \times \boldsymbol{\omega}, \quad (\text{S15})$$

where \mathbf{u} , \mathbf{R} , and $\boldsymbol{\omega}$ are the translational velocity, center of mass, and angular velocity of the suspended particles, respectively. The resultant hydrodynamic force on each suspended particle \mathbf{F}^h is the sum of all forces on the cells inside the particle l as $\mathbf{F}^h = \sum_{\mathbf{r} \in l} \tilde{\mathbf{F}}_{\text{cell}}(\mathbf{r})$. Similarly, the torque is given by $\mathbf{T}^h = \sum_{\mathbf{r} \in l} (\mathbf{r} - \mathbf{R}) \times \tilde{\mathbf{F}}_{\text{cell}}(\mathbf{r})$. Note that this method requires a contribution to the body force density of the fluid $\tilde{\mathbf{f}}$. Therefore, we calculate $\tilde{\mathbf{f}}$ in Eqs. (S6) and (S5) as

$$\tilde{\mathbf{f}}(\mathbf{r}) = -\rho_f g \hat{\mathbf{z}} - \frac{\tilde{\mathbf{F}}_{\text{cell}}(\mathbf{r})}{\Delta x^3}. \quad (\text{S16})$$

Note that the first term comes from the gravity.

II. ADDITIONAL FIGURES

In this section, we present several figures that are not placed in the main text. First, we plot the force exerted on the impactor for $\phi = 0.54$ and $u_{0,z}^I/u^* = 1.61$ in Fig. S2, when the impactor does not bounce. In contrast to Fig. 1(c) in the main text, no distinct peak exists in $F_{I,z}$ in this case. Moreover, there is a visible time delay between the maximum hydrodynamic contribution and the maximum contact contribution. It is easy to imagine that this response is viscous not to make the impactor rebounds.

Normal displacement. In Fig. S3(a), we visualize the particle displacement in normal (z -) direction Δz , sliced in the middle of the simulation box. Here, one can observe the existence of localized region of high normal displacements, which corresponds to the dynamically jammed region. Note that our observation is similar to the displacement field observed in an experiment of rod impactor [S13].

Shear stress. In Fig. S3(b), we visualize the dimensionless shear stress on each suspended particle σ_{xz}/σ_0 , with $\sigma_0 = \frac{4}{3}\pi\rho_f a_{\min} g$, sliced in the middle of the simulation box. Here, one can observe that the magnitude of the shear stress is almost uniform. This indicates that the shear stress plays a minor role in the impact problem because it is unrelated to the force chains (Fig. 3(b) in the main text). We also visualize the absolute ratio between the shear and normal stress $|\sigma_{xz}/\sigma_{zz}|$ in Fig. S3(c), which shows that the shear stress is much smaller than the normal stress. This clarifies another difference between the impact problem and the DST in which the shear stress is as large as the normal stress.

-
- [S1] Pradipto, Master Thesis, Kyoto University (2019).
[S2] Pradipto and H. Hayakawa, Simulation of dense non-brownian suspensions with the lattice boltzmann method: shear jammed and fragile states, *Soft Matter* **16**, 945 (2020).
[S3] A. J. C. Ladd, Numerical simulations of particulate sus-

- pensions via a discretized boltzmann equation. part 1. theoretical foundation, *J. Fluid Mech* **271**, 285 (1994).
[S4] A. J. C. Ladd, Numerical simulations of particulate suspensions via a discretized boltzmann equation. part 2. numerical simulations, *J. Fluid Mech* **271**, 311 (1994).
[S5] A. Leonardi, Ph.D Thesis, ETH Zurich (2015).

- [S6] S. Succi, *The lattice Boltzmann equation: for fluid dynamics and beyond* (Oxford University Press, 2001).
- [S7] P. L. Bhatnagar, E. P. Gross, and M. Krook, A model for collision processes in gases. i. small amplitude processes in charged and neutral one component systems, *Phys. Rev.* **94**, 511 (1954).
- [S8] Z. Guo, C. Zheng, and B. Shi, Discrete lattice effects on the forcing term in the lattice boltzmann method, *Phys. Rev. E.* **65**, 046308 (2002).
- [S9] C. Korner, M. Thies, T. Hofmann, N. Thurey, and U. Rude, Lattice boltzmann model for free surface flow for modeling foaming, *J. Stat. Phys.* **121**, 179 (2005).
- [S10] O. Švec, J. Skocek, H. Stang, M. R. Geiker, and N. Roussel, Free surface flow of a suspension of rigid particles in a non-newtonian fluid: A lattice boltzmann approach, *J. Non-Newton. Fluid.* **179-180**, 32 (2012).
- [S11] A. Leonardi, M. Cabrera, F. K. Wittel, R. Kaitna, M. Mendoza, W. Wu, and H. J. Herrmann, Granular-front formation in free-surface flow of concentrated suspensions, *Phys. Rev. E.* **92**, 052204 (2015).
- [S12] C. S. Peskin, Flow patterns around heart valves: A numerical method, *J. Comput. Phys.* **10**, 252 (1972).
- [S13] S. R. Waitukaitis and H. M. Jaeger, Impact-activated solidification of dense suspensions via dynamic jamming fronts, *Nature* **487**, 205 (2012).